Solar RRL
www.solar-rrl.com

Minimizing Open-Circuit Voltage Losses in Perovskite/Perovskite/Silicon Triple-Junction Solar Cell with Optimized Top Cell

Minasadat Heydarian, Athira Shaji, Oliver Fischer, Michael Günthel, Orestis Karalis, Maryamsadat Heydarian, Alexander J. Bett, Hannes Hempel, Martin Bivour, Florian Schindler, Martin C. Schubert, Andreas W. Bett, Stefan W. Glunz, Juliane Borchert, and Patricia S. C. Schulze*

Following the impressive efficiencies achieved for two-terminal perovskite/silicon dual–junction solar cells, perovskite/perovskite/silicon triple-junction cells have now gained attention and are rapidly developing. In a two-terminal triple-junction cell, maximizing the open-circuit voltage (V_{OC}) is not straightforward as it requires understanding and mitigating the dominant losses in such a complex structure. Herein, the high bandgap perovskite top cell is first identified as the main source of the V_{OC} loss in the triple-junction cell. A multifaceted optimization approach is then implemented that improves the V_{OC} of the 1.83 eV perovskite. This approach consists of 1) replacing the reference triple-cation/double-halide with a triple-cation/triple-halide perovskite, which improves perovskite bulk quality and reduces transport losses, and 2) implementing a piperazinium iodide passivation between the perovskite and the electron transport layer, which reduces nonradiative recombination losses at this interface. Employing these optimizations in the top cell of the triple-junction boost the V_{OC} by average 124 mV. A high V_{OC} of more than 3.00 V is achieved with a fill factor of 79.6%, a short-circuit current density of 9.0 mA cm^{-2}, and an efficiency of 21.5%. Further study is conducted on the improvement of V_{OC} in the triple-junction solar cell using subcell selective photoluminescence-based implied V_{OC} imaging, which is applied for the first time to a perovskite-based triple-junction structure.

1. Introduction

Within recent years of development, perovskite/silicon dual-junction solar cells have shown remarkable improvement in power conversion efficiency (*PCE*) by up to 34.6%.[1,2] Even further enhancement of *PCE* is possible by the addition of a hird junction. Recently, the two-terminal perovskite/perovskite/silicon triple-junction structure has gained increasing attention with first device demonstrations.[3–10] In a two-terminal multijunction solar cell, since the photon flux is split between the subcells, the total current is lowered and limited by the current of the subcells. On the other hand, high voltage is the main characteristic of these devices. As the voltages from the different subcells add up to ensure the highest voltage delivered by a triple-junction device, it is essential to minimize voltage losses in individual subcells and optimize their electrical interconnection.

Tackling the limited V_{OC} in a triple-junction solar cell, however, is not trivial as there are many sources of losses and thus identifying them in such a complex system is challenging. Nevertheless, the high bandgap perovskite top cell is known to be

M. Heydarian, A. Shaji, O. Fischer, M. Günthel, M. Heydarian, A. J. Bett, M. Bivour, F. Schindler, M. C. Schubert, A. W. Bett, S. W. Glunz, J. Borchert, P. S. C. Schulze
Fraunhofer Institute for Solar Energy Systems ISE
Heidenhofstraße 2, 79110 Freiburg, Germany
E-mail: Minasadat.Heydarian@ise.fraunhofer.de

The ORCID identification number(s) for the author(s) of this article can be found under https://doi.org/10.1002/solr.202400645.

DOI: 10.1002/solr.202400645

M. Heydarian, O. Fischer, S. W. Glunz, J. Borchert
Department of Sustainable Systems Engineering
Chair for Photovoltaic Energy Conversion
University of Freiburg
Emmy-Noether-Straße 2, 79108 Freiburg, Germany

A. Shaji, A. W. Bett
Institute of Physics
University of Freiburg
Hermann-Herder-Straße 3, 79104 Freiburg, Germany

O. Karalis, H. Hempel
Solar Energy Devision
Helmholtz-Zentrum Berlin
Hahn-Meitner-Platz 1, 14109 Berlin, Germany

one of the main drivers dominating the V_{OC} loss in a perovskite/perovskite/silicon triple-junction solar cell. Based on simulations, the top cell of a triple-junction solar cell requires a high bandgap in the range of 1.8–2.0 eV.[11] To achieve such a high bandgap perovskite with a multication multihalide perovskite, the amount of bromine (Br) needs to be increased. However, solar cells with high bandgap perovskite compositions containing more than 20% Br commonly exhibit a high V_{OC} deficit with respect to their theoretical V_{OC},[12] which limits their performance. This mainly originated from photoinduced phase segregation,[13] nonradiative recombination losses in the perovskite bulk and at the interfaces,[14] and band misalignment with commonly used charge transport layers.[15]

Additive engineering is one of the most common approaches to improve the perovskite bulk quality. For example, chloride (Cl)-based additives have widely been reported to improve the quality of the high bandgap perovskite absorber and reduce defect density.[16] In this approach, Cl is typically not incorporated into the final perovskite crystal lattice. Cl instead plays a role during the film formation process by influencing the crystallization dynamics and is mostly removed from the film during the annealing step.[16] Xu et al. were the first to report on a triple-halide perovskite with a bandgap of 1.67 eV where chloride is incorporated into the perovskite lattice resulting in an increase in charge carrier lifetime and reduction in V_{OC} deficit.[17] Recently, triple-halide perovskite has been studied and used as a top cell in all-perovskite[18] and perovskite/silicon dual-junction applications.[19,20]

Furthermore, besides the quality of the absorber layer, the perovskite/C_{60} interface has been shown to be one of the main sources of V_{OC} loss in high bandgap perovskites.[21] This is due to the high nonradiative recombination losses at this interface[14] and nonideal band alignment of this charge transport layer with the high bandgap perovskite.[15,22] Various passivation strategies have been implemented at this interface to reduce the nonradiative recombination loss and improve the V_{OC}. For example, for perovskites with a bandgap of more than 1.8 eV, materials such as lithium fluoride (LiF)[23] and propane-1,3-diammonium iodide (PDAI)[24] have been shown to effectively passivate the perovskite/electron transport layer (ETL) interface. Recently, piperazinium iodide (PI) has been used in combination with triple-halide perovskite compositions to enhance V_{OC} of the top cell in perovskite/silicon and all-perovskite tandem solar cells.[18,19]

In this work, we first identify the dominant source of voltage loss in our perovskite/perovskite/silicon triple-junction solar cell, which is the high bandgap perovskite top cell. We then aim to reduce the V_{OC} loss in our top cell. For this purpose, we employ a multifaceted strategy consisting of 1) replacing the reference triple-cation/double-halide perovskite with triple-cation/triple-halide perovskite composition and 2) implementing a PI passivation between the perovskite and the electron transport layer. By systematic characterization of perovskite films, half stacks, single-junction, and finally triple-junction solar cells, we show how these steps improve the perovskite bulk quality and interface, leading to improvement of V_{OC} in both single-junction and triple-junction solar cells.

2. Results and Discussion

The starting point of this work was our previously reported triple-junction solar cell[7] which has a top cell composed of a triple-cation perovskite, $Cs_{0.05}(FA_{0.55}MA_{0.45})_{0.95}Pb(I_{0.55}Br_{0.45})_3$, with a bandgap of 1.83 eV, and a middle cell with the $Cs_{0.05}(FA_{0.90}MA_{0.10})_{0.95}Pb(I_{0.95}Br_{0.05})_3$ composition, with a bandgap of 1.56 eV. Even though the V_{OC} of 2.87 V achieved for this triple-junction solar cell was equal to the sum of the voltages of the individual subcells determined from single-junction structures, it is still below the practical voltage potential for this structure. According to simulations, a perovskite/perovskite/silicon triple-junction solar cell has a radiative V_{OC} potential of 3.7 V which cannot be achieved in practice.[25] A more realistic scenario by taking the optical and electrical losses into account predicted a practical V_{OC} potential of 3.2 V.[26]

First, to identify which subcell mainly contributes to the V_{OC} limitation in our structure, the individual subcells were separately studied. For this purpose, half stacks and single-junction solar cells of the high bandgap perovskite top cell and the middle bandgap perovskite middle cell were prepared. **Figure 1**

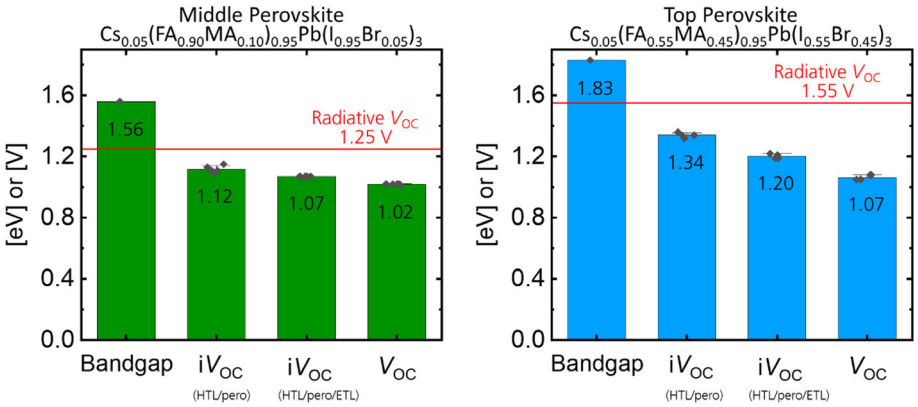

Figure 1. Comparison of bandgap derived from Tauc plot (from reflection transmission measurements on glass/ITO/HTL/perovskite), implied open-circuit voltage (iV_{OC}) derived from PLQY measurement of a glass/ITO/HTL/perovskite stack with and without ETL, the measured V_{OC} for single-junction perovskite middle cells (bandgap 1.56 eV) (left) and top cells (bandgap 1.83 eV) (right) of our previously reported perovskite/perovskite/silicon triple-junction solar cell.[7] V_{OC} deficit of high bandgap perovskite with respect to the radiative limit,[12] as well as iV_{OC} to V_{OC} loss, is higher for the top than the middle subcell. The bar charts of statistical data show the mean values and the upper lines represent the standard deviation.

compares the radiative V_{OC}, implied V_{OC} (iV_{OC}) measured on the perovskite films and after ETL deposition with the device V_{OC} of corresponding single-junction solar cells for the perovskite middle cell and top cell with respect to their bandgaps.

Comparison of the potential radiative V_{OC} of 1.56 and 1.83 eV solar cells[12] and the average V_{OC} of their respective single-junction solar cells (Figure S1, Supporting Information) shows a V_{OC} deficit of 480 mV for the high bandgap top cell, which is more than double compared to the middle cell (230 mV). In addition, the iV_{OC} values derived from photoluminescence quantum yield (PLQY) measurements on the glass/indium tin oxide (ITO)/hole transport layer (HTL)/perovskite stacks were compared with the iV_{OC} after ETL deposition. The iV_{OC} loss after the ETL deposition is more pronounced for the high bandgap perovskite. Finally, the iV_{OC} to V_{OC} loss is 50 mV for the middle bandgap perovskite, while the high bandgap perovskite exhibits a loss of 130 mV. Therefore, in this work, we focus on reducing the V_{OC} loss in the high bandgap perovskite subcell.

2.1. Improving the Bulk Quality of the High Bandgap Perovskite Absorber

Here, high bandgap triple-cation/double-halide perovskite $Cs_{0.05}(FA_{0.55}MA_{0.45})_{0.95}Pb(I_{0.55}Br_{0.45})_3$ (reference) and triple-cation/triple-halide perovskite compositions are compared, hereafter abbreviated as 3C2H and 3C3H, respectively. In order to achieve a triple-halide perovskite composition, 10 mol% $MAPbCl_3$ is added to a base double-cation/double-halide perovskite $(Cs_{0.22}FA_{0.78})Pb(I_{0.70}Br_{0.30})_3$ as previously reported by.[17–20,24] The composition is estimated to be $Cs_{0.20}FA_{0.71}MA_{0.09}Pb(I_{0.64}Br_{0.27}Cl_{0.09})_3$. Additionally, we checked this composition through depth profiling XPS measurements which confirmed the expected perovskite composition. Detail about XSP measurement will be discussed later and more information can be found in Table S3, Supporting Information.

For the 3C3H composition, we targeted a bandgap similar to our reference 3C2H perovskite (1.83 eV). Tauc analysis obtained from reflection and transmission (RT) measurements revealed a similar bandgap for both perovskite compositions (Figure S2b, Supporting Information). As can be seen from Figure S2a, Supporting Information, the absorption in the wavelength range of 550–650 nm is higher for the 3C3H perovskite. This can be attributed to the higher thickness of this absorber as evidenced by cross-sectional scanning electron microscopy (SEM) images (Figure S2c, Supporting Information). The 3C2H perovskite film has an average thickness of 260 nm while the 3C3H absorber shows an average thickness of 360 nm. It should be noted that perovskite solution concentration (1 M) and processing parameters are kept similar. The difference in thickness could be attributed to varying crystallization behavior of the different perovskite compositions. The different film formation is also obvious from the top view SEM images presented in Figure S2d, Supporting Information.

To study the incorporation of Cl into the 3C3H perovskite lattice, we first prepared a base double-cation composition of $(Cs_{0.22}FA_{0.78})Pb(I_{0.70}Br_{0.30})_3$ prior to adding $MAPbCl_3$. The bandgap obtained from the Tauc plot is 1.76 eV, which aligns with the photoluminescence (PL) peak position of ≈700 nm. Upon adding the $MAPbCl_3$ to the base double-cation solution, the bandgap shifted to 1.83 eV corresponding to a 0.08 eV increase (Figure S3a,b, Supporting Information) agreeing well with,[17] where they tuned the bandgap from 1.65 to 1.90 eV with different Br and Cl contents. This change in the bandgap confirms the incorporation of Cl into the perovskite lattice. As Cl has a smaller ionic radius compared to bromide (Br) and iodide (I) (I: 2.20 Å > Br: 1.96 Å > Cl: 1.81 Å),[27] its incorporation into the perovskite lattice results in a change in lattice constant and an increase of the bandgap. The change in lattice constant can also be seen in the XRD measurement of the perovskite films before and after adding $MAPbCl_3$ (Figure S3c, Supporting Information).

Energy-dispersive X-ray spectroscopy (EDX) measurements of 3C3H films further confirmed the presence of Cl (Figure S4, Supporting Information) in our perovskite. In addition, depth-profiling X-ray photoemission spectroscopy (XPS) measurements were conducted on both reference 3C2H perovskite and 3C3H perovskite films. The XPS spectra for Br 3*d*, I 3*d*, and Cl 2*p* are presented in **Figure 2**a, along with their stoichiometric ratios at different sputtering times (Figure 2b).

As expected for the 3C2H perovskite, no Cl could be detected, whereas, for the 3C3H perovskite the detailed photoelectron spectrum in the Cl 2p region shows a clear Cl signal. XPS spectra were recorded at the surface and after sputtering for 6000 and 12 000 s into the perovskite film, corresponding to depths of ≈100 and 200 nm, respectively (see Figure S5, Supporting Information). As shown in Figure 2b, for the 3C2H perovskite, the halide distribution remains relatively constant until 100 nm depth. From 100 to 200 nm depth of the films, the distribution changes significantly for the 3C2H perovskite composition, while it changes less drastically for the 3C3H composition. This suggests that the presence of Cl helps to maintain a more consistent distribution of halides within the 3C3H perovskite film. The XRD spectra of 3C2H and 3C3H perovskite films are presented in **Figure 3**a. Both compositions show diffraction peaks at 13.9°, 19.8°, 24.3°, 28.15°, and 31.55° corresponding to the (110), (112), (211), (220), and (310) planes.[28–30] Additionally, due to a lead halide excess present in the precursor solution (see the Experimental Section), both XRD patterns exhibit a peak corresponding to PbI_2 at 12.5°. The most obvious difference in the XRD patterns of the two perovskites is the preferred orientation toward the (112) plane for the 3C3H perovskite while the 3C2H perovskite composition shows preferential orientation toward (110) plane. This change in crystal orientation has not been reported in the previous publications on 3C3H absorber.[16–19] However, it is important to note that the perovskite deposition method used here is dynamic gas quenching (GQ), which is adapted for top cell processing for triple-junction solar cells[7] and is different from the standard static spin coating and antisolvent method used in the other mentioned works.

In order to investigate whether this change originates from the deposition technique, we deposited the 3C3H perovskite with the standard antisolvent method and performed XRD measurements (Figure S6, Supporting Information). The comparison of the XRD patterns shows that the change was indeed affected by the dynamic GQ method used for the deposition. However, this is not independent from the perovskite composition as employing the dynamic GQ method previously did not show such change in the crystallization of 3C2H perovskite.[7] Comparing

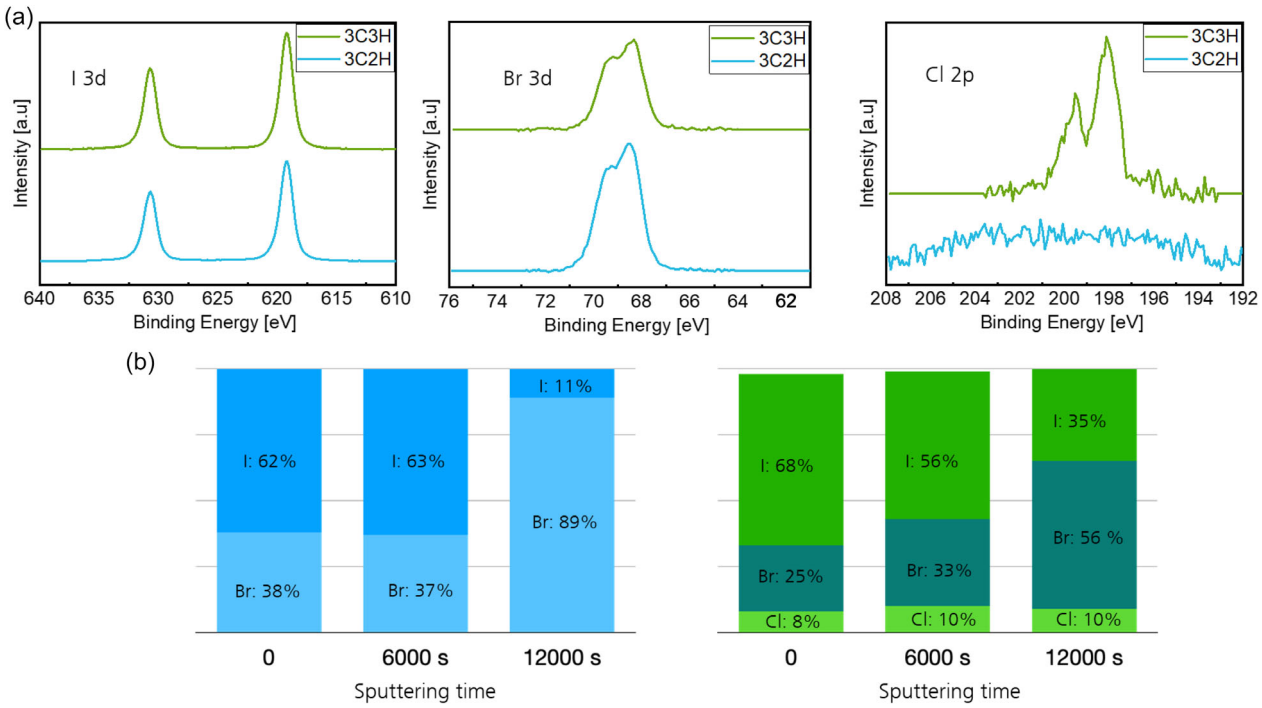

Figure 2. a) XPS spectra of Br 3 *d*, I 3 *d*, and Cl 2*p* indicating the presence of Cl in the 3C3H absorber and b) their respective stoichiometric ratios at sputtering time of 0, 6000, and 12 000 s for 3C2H and 3C3H perovskites. Cl is only presented in the 3C3H composition, and its amount is constant throughout the film.

the XRD patterns of the base double-cation composition $(Cs_{0.22}FA_{0.78})Pb(I_{0.70}Br_{0.30})_3$ prior to adding $MAPbCl_3$ (Figure S3c, Supporting Information) indicates that the orientation change is not related to the presence of Cl in the perovskite. As previous publications have shown that highly Cs-doped perovskites generally exhibit preferred orientation along (112),[28,31] we conclude that the observed change is the result of the combination of the GQ deposition method with the high cesium (Cs) content in the target 3C3H composition.

To study the effect of this change in the perovskite crystallization on the optoelectronic properties of our perovskite, we performed transient photoluminescence (TrPL) measurements to study the carrier lifetime (τ) in respective thin film stacks. From Figure 3b, the 3C3H perovskite film shows a longer charge carrier lifetime (121 ns) compared to the 3C2H reference composition (70 ns). To confirm the origin of this improved charge carrier lifetime, we performed PLQY measurement on the same samples. From this measurement, the iV_{OC} of the 3C3H absorber is 40 mV higher than the one of the reference 3C2H perovskite (Figure 3c). As the PLQY measurement is the direct relation of the radiative recombination to the total recombination, this improved iV_{OC} is an indication of reduced nonradiative recombination losses in the perovskite bulk, which we refer to an improved bulk quality with less trap density. This is in line with the previous reports that show promoted charge transport within the perovskite films, as well as suppressed trap states when the perovskite crystal is oriented along the 112 plane.[28–30,32]

Next, we measured iV_{OC} of these two perovskites on glass/ITO/2PACz/perovskite/C_{60}/SnO_x stacks. Upon deposition of C_{60}/SnO_x, overall, there is a reduction in iV_{OC} compared to the measurements on bare perovskite films for both absorbers (0.14 V for 3C2H and 0.17 V for 3C3H) and iV_{OC} of 3C3H is only 10 mV higher than the one of 3C2H (Figure 3d). This improvement is less than the 40 mV improvement observed on perovskite films before C_{60}/SnO_x deposition. This is due to the fact that the nonradiative recombination loss at the perovskite/ETL interface dominates the loss; the benefit from absorber improvement is not obvious anymore.[14] Therefore, the nonradiative recombination at this interface needs to be reduced to fully benefit from the absorber improvement.

2.2. Improving the Perovskite/C_{60} Interface

After improving the bulk quality of the high bandgap perovskite absorber, we aimed to minimize the nonradiative recombination loss at the perovskite surface and interface to the ETL. For surface passivation, we treated the 3C3H perovskite surface with PI similar to the approach previously reported by Li et al. for single-junction perovskite solar cells,[33] Mariotti et al. for perovskite/silicon tandem solar cells,[19] and Yang et al. for all-perovskite tandems.[18] For this purpose, PI dissolved in IPA (0.4 mg mL^{-1}) was spin coated on the perovskite layer and annealed afterward. It is worth mentioning that in all the previously mentioned studies, the standard antisolvent method was used to process the perovskite layer. In contrast, our work employs a dynamic deposition technique combined with GQ, which leads to a different perovskite crystallization and morphology as explained in Section 2.1. Therefore, it is necessary to study the effect of PI passivation, as

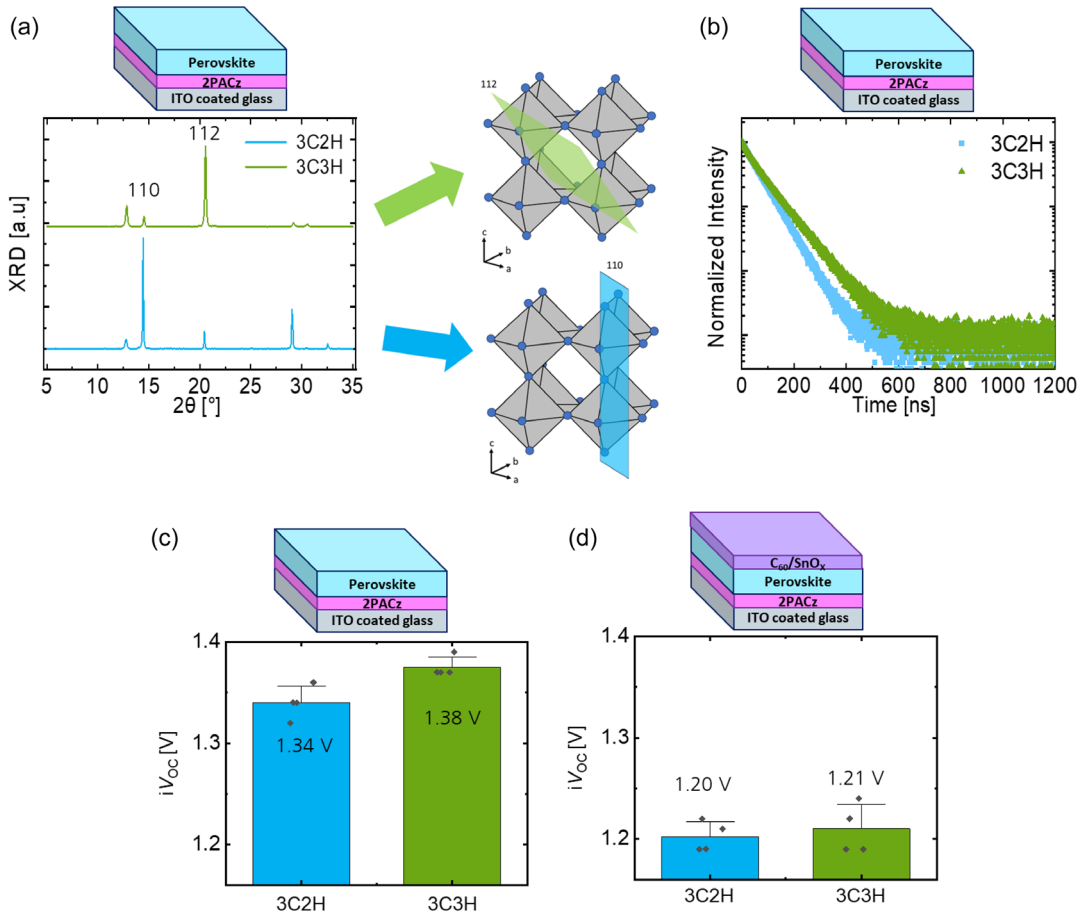

Figure 3. a) XRD patterns of 3C2H and 3C3H perovskite compositions measured on a glass/ITO/HTL/perovskite stack showing a different preferred crystal orientation for the 3C3H absorber compared to the 3C2H. b) TrPL measurement on glass/ITO/HTL/perovskite stacks for 3C2H and 3C3H perovskite indicating longer carrier lifetime for the 3C3H, and c) their corresponding iV_{OC} values derived from PLQY measurements. 3C3H absorber gives a higher value. d) iV_{OC} comparison after deposition of C_{60}/SnO_x layers results in only a 10 mV difference. The bar charts of statistical data show the mean values and the upper lines represent the standard deviation.

the interaction between the passivation layer and the perovskite surface could differ significantly, potentially leading to unique enhancements or challenges.

The effect of PI treatment on the crystallinity of our perovskite was examined by XRD measurement (**Figure 4**a). In this study, no noticeable change in the XRD pattern was observed after treating the surface with PI. The diffraction peaks are similar, and no formation of a low dimensional phase is observed (Figure 4a) in line with previous reports. However, the PI passivation alters the surface of the perovskite as observed in XPS analysis (Figure 4b); an additional lead species can be identified in the Pb 4f photoelectron spectrum after the passivation step. The 3C3H perovskite shows a Pb 4f7/2 signal at a binding energy of 138.4 eV; the passivated perovskite 3C3H + PI shows two signals, the same species at a binding energy of 138.5 eV and another one at 139.3 eV. This additional species must be related to an interaction between the nitrogen functions of the piperazinium molecules and the lead in the perovskite structure.[34] Also, the N 1s spectrum shows a diversity of N-functions including PI signals and a potential species related to a PI-lead interaction. To confirm this, an XPS measurement of pristine PI powder was performed and compared to 3C3H + PI. Three distinguishable signals in the N 1s region of PI (Figure S7, Supporting Information) can be assigned to a protonated species (402.5 eV) and nonprotonated species (400.0 and 401.0 eV). The XPS measurement on 3C3H + PI shows an additional fourth species at a binding energy of 400.4 eV. This nitrogen signal can be assigned to either a nitrogen function of the perovskite or a nitrogen function of PI in interaction with lead, which would explain the additional lead species at higher binding energy. The XPS data of the C 1s, N 1s, and Pb 4f7/2 signals for 3C2H, 3C3H, and 3C3H + PI on the respective samples' surface and after sputtering of 6000 s are shown in Table S2, Supporting Information. After the sputtering step, no differences between the samples can be observed anymore, which demonstrates that the passivation treatment with PI only affects the surface of the perovskite and not the entire bulk. This can also be seen from the corresponding XPS spectra for 3C3H and 3C3H + PI plotted in Figure 4b.

Moreover, iV_{OC} measured on glass/ITO/2PACz/perovskite stacks are almost similar for the PI-treated sample and the

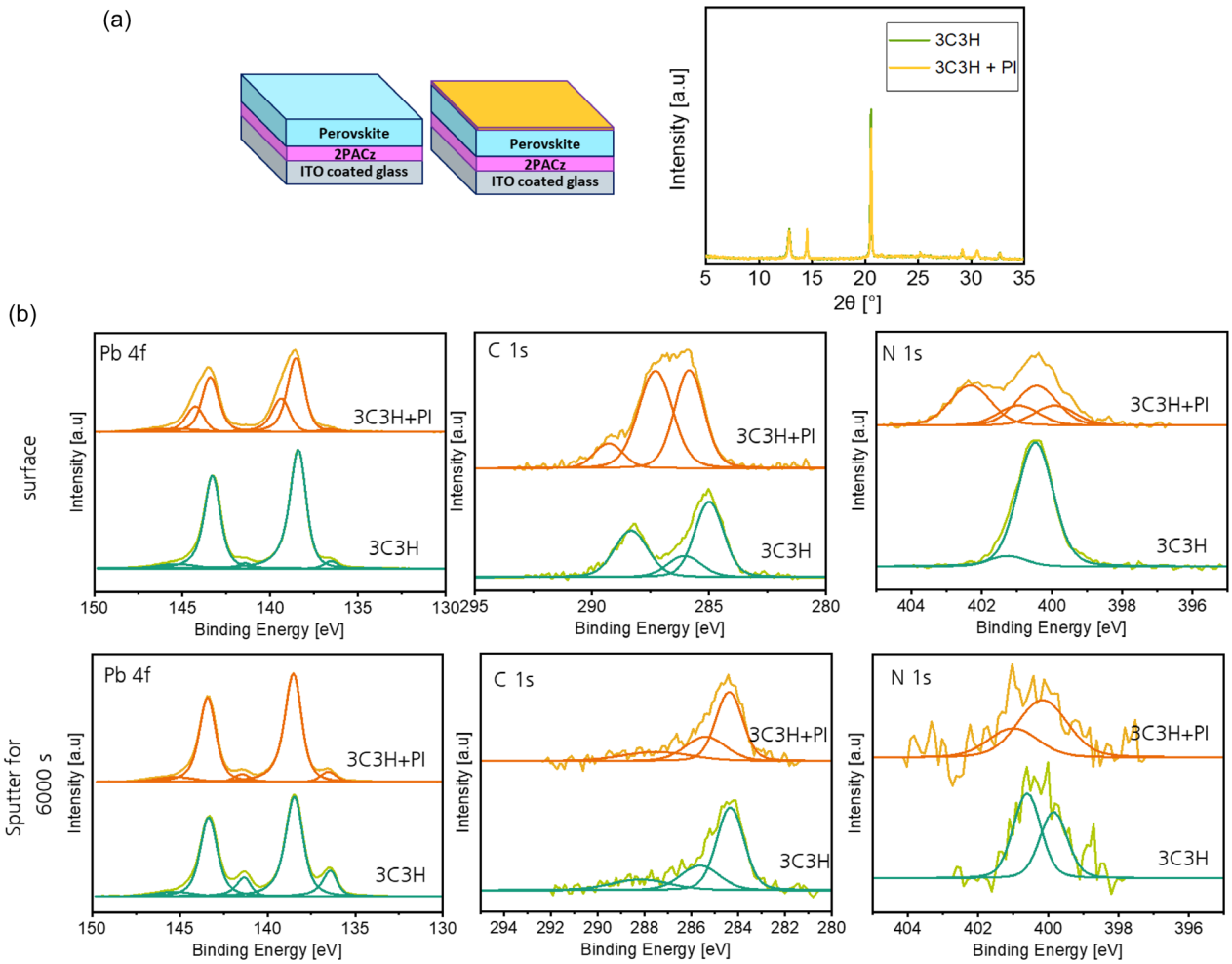

Figure 4. a) XRD patterns of 3C3H perovskite before and after PI treatment show similar patterns. b) Pb4f, C1s, and N1s XPS spectra of the 3C3H absorber with and without PI passivation for sputtering times of 0 and 6000 s corresponding to surface and 100 nm depth of the films, respectively. PI affects the surface of the perovskite and not the bulk.

nontreated sample (**Figure 5**a). Hence, PI does not show a passivation effect on the surface of the perovskite and does not affect the bulk quality of the perovskite. We then performed the same measurement after deposition of the C_{60}/SnO_x. As shown in Figure 5b, after ETL deposition, iV_{OC} of the PI-treated sample is 40 mV higher than that of the nontreated sample. Thus, PI passivation successfully reduced the nonradiative recombination at the mentioned interface.

In order to compare the device performance of 3C3H high bandgap perovskite with our reference 3C2H perovskite and the effect of PI passivation, we fabricated semitransparent single-junction perovskite solar cells with a glass/ITO/2PACz/perovskite/C_{60}/SnO_x/ITO/Ag/MgF_2 structure. The statistics of the photovoltaic parameters (*PCE*, fill factor (*FF*), j_{SC}, and V_{OC}) measured from the MgF_2 side are shown in **Figure 6**b. Single-junction solar cells with 3C3H absorber show average 70 mV enhancement in V_{OC} compared to the reference 3C2H absorber. This is partially attributed to the improved perovskite bulk quality; however, as discussed in Section 2.1, the dominant losses at the perovskite/C_{60} interface limit the V_{OC} improvement (Figure 3d).

To get more insight into the origin of this V_{OC} improvement, transient surface photovoltage (trSPV) measurements were performed on glass/ITO/HTL/perovskite/C_{60}/SnO_x stacks to study the charge carrier extraction dynamic of 3C2H and 3C3H absorbers (Figure 6d). The SPV transients start from an amplitude of 0, as we subtracted the photovoltage before the arrival of the laser pulse (i.e., the photovoltage from previous laser pulses and ambient light). Hence, we refer to the *y*-axis as "ΔSPV" rather than "SPV." Figure 6d exhibits negative SPV signals for both samples, indicating an excess of negative charge on the surface of the sample and positive charge at the back. This is expected for p–*i*–*n* solar cells, where electrons migrate toward the surface (ETL-side) and holes toward the bottom of the sample (HTL-side). The 3C3H absorber exceeds the SPV amplitude of the 3C2H, indicating better charge extraction for 3C3H compared to the 3C2H.[35]

Upon treating the 3C3H perovskite surface with PI, the average V_{OC} further improved to 1.21 V, corresponding to 94 mV improvement. This improvement results from the reduction of nonradiative recombination loss at perovskite/ETL interface as evidence by the observed iV_{OC} improvement after ETL

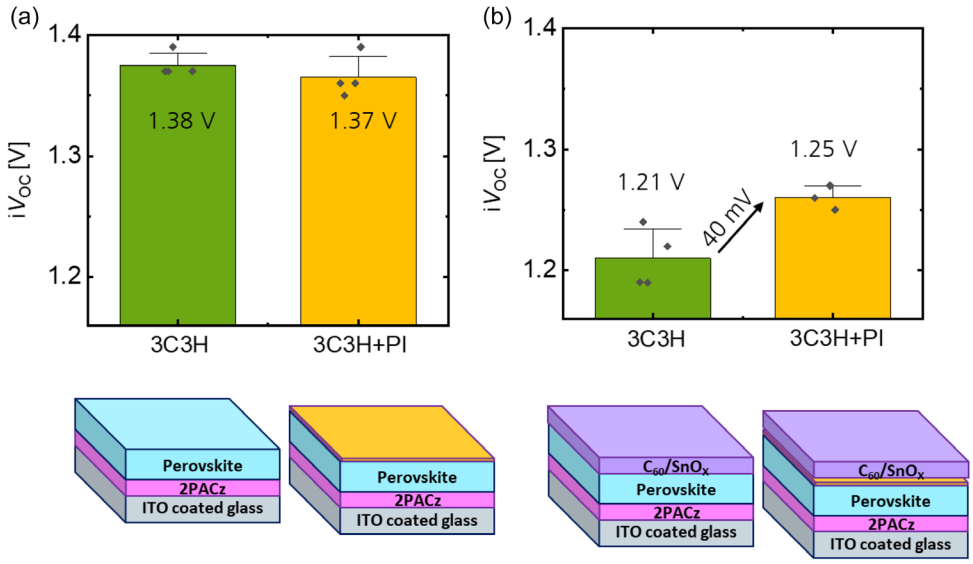

Figure 5. a) iV_{OC} values from measurements on glass/ITO/HTL/perovskite stack before and after PI treatment are the same and b) iV_{OC} values from measurements on glass/ITO/HTL/perovskite/C60/SnO_x stack with and without PI treatment show improvement after the PI treatment.

deposition. This improvement in V_{OC} however is more than that observed in the iV_{OC}. In order to study whether this improvement is also attributed to improved charge extraction, we performed trSPV measurement on the glass/ITO/HTL/Perovskite/C_{60}/SnO_x stacks for samples with and without PI passivation. Agreeing well with the previous reports,[19] PI treatment impacts the charge extraction (Figure 6d) and the PI-treated sample shows more negative SPV signal compared to the nontreated sample. Therefore, the improved V_{OC} by PI passivation originated from both reduction in nonradiative recombination loss and better charge extraction. This improved charge extraction in the presence of PI passivation can be attributed to better energetic band alignment with C_{60}, which was reported in previous publications.[19,33] The average *FF* and j_{SC} remain within the same range; the *PCE* follows the same trend as the $V_{OC;}$ and the highest *PCE* is achieved for samples with 3C3H perovskite absorber in combination with PI passivation.

2.3. Implementation in Triple-Junction Solar Cells

Finally, to assess the impact of the described top cell optimization on the performance of our perovskite/perovskite/silicon triple-junction solar cells, we fabricated devices with 1 cm^2 active area and the structure shown in **Figure 7**a with different perovskite top cells. We compared our reference high bandgap 3C2H perovskite with the 3C3H perovskite composition and a combination of 3C3H and PI passivation. The corresponding *jV* curves of these devices, fabricated in the same batch, are presented in Figure S8, Supporting Information. The trend of V_{OC} improvement aligns well with the results of single-junction solar cells. Notably, the triple-junction solar cells with the 3C3H perovskite top cell reached a V_{OC} of 2.90 V, showing an absolute enhancement of 50 mV compared to the control device. This V_{OC} was further increased to 2.95 V with the implementation of PI passivation at perovskite/C_{60} interface. To verify the reproducibility of the improvements, device statistics comparing the reference and optimized high bandgap perovskite (3C3H + PI) from different batches are plotted in Figure S9a, Supporting Information, which confirmed an average 124 mV improvement in the V_{OC} upon implementation of the optimized high bandgap top cell; champion devices with V_{OC} of more than 3.00 V were achieved. This is among the highest values reported in the literature for this structure (Figure S9b, Supporting Information).

After improving V_{OC} of our device, we implemented a silver grid mask with ≈5% reduced shading (Figure S10, Supporting Information), which led to a 0.5 mA cm^{-2} increase in j_{SC} of the triple-junction solar cell. The champion device with the new grid design and the optimized top cell absorber (3C3H perovskite +PI passivation) demonstrates a *PCE* of 21.5% with a j_{SC} of 9.0 mA cm^{-2}, V_{OC} of 3.00 V, and *FF* of 79.6% under reverse scan direction and *PCE* of 21.3% measured at fixed voltage for 600 s. Figure 7 presents the *jV* curve of this cell together with its corresponding external quantum efficiency (*EQE*) and cross-sectional SEM image. The triple-junction solar cell was stable and retained 95% of its initial *PCE* after more than 13 h measurement at a fixed voltage close to maximum power point in ambient environment with a relative humidity of ≈50% without any encapsulation (Figure S11, Supporting Information).

2.4. Subcell Analysis of Triple-Junction Solar Cells

To understand the origin of improvements and/or losses in a multijunction solar cell, it is important not only to evaluate the performance of the single- and multijunction solar cells, but also to characterize the individual subcells within the final device. Given the complex fabrication sequence of multijunction solar cells, the quality and properties of subcells may differ from those of single-junction devices made from the same materials. Therefore, a subcell-selective analysis within multijunction

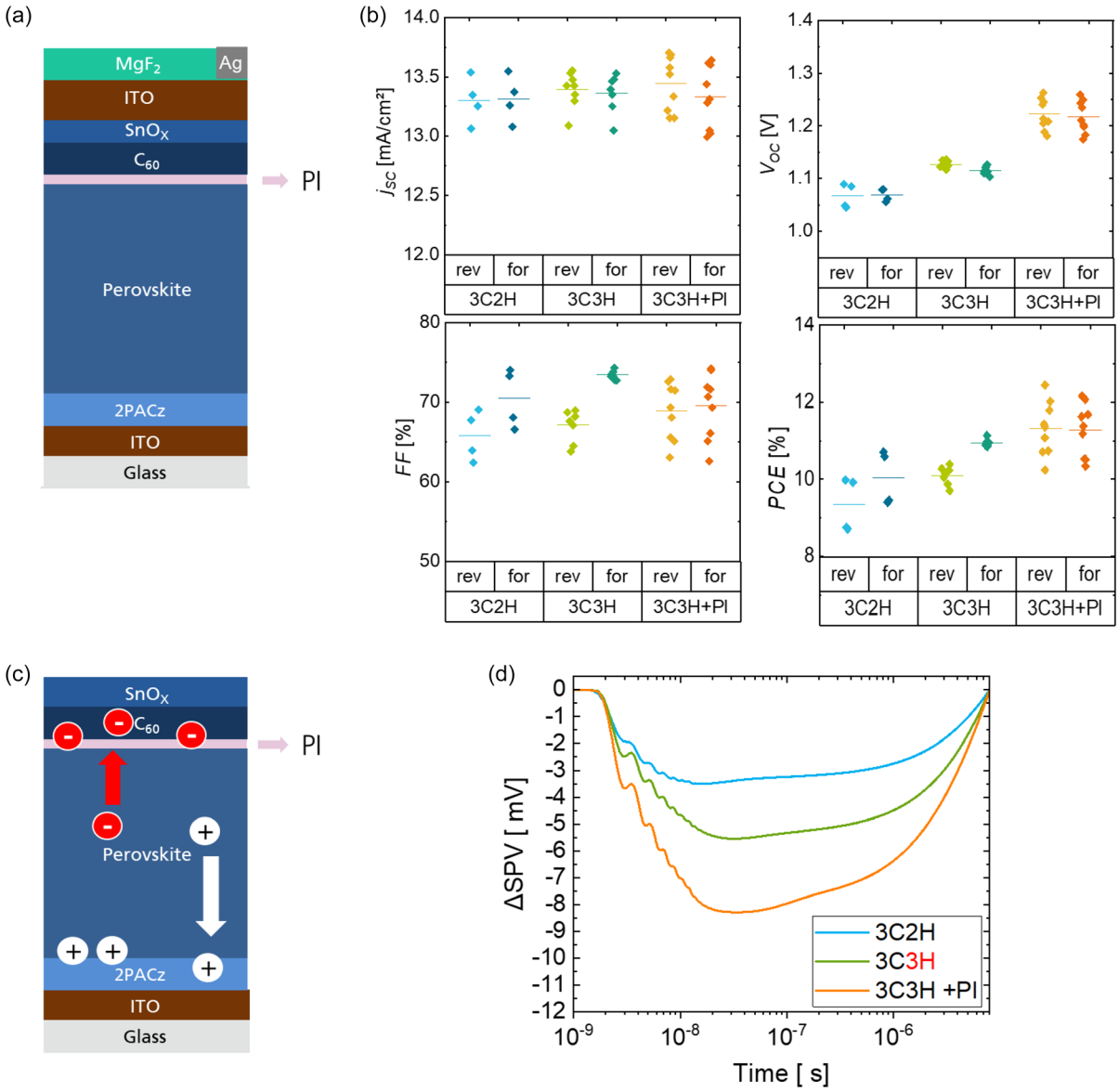

Figure 6. a) Schematic diagram of semitransparent single-junction solar cells. b) Photovoltaic parameters (j_{SC}, V_{OC}, *FF*, and *PCE*) of single-junction solar cells for 3C2H absorber, 3C3H absorber, and 3C3H absorber with PI passivation. Solar cells with 3C3H absorber have higher V_{OC} compared to 3C2H and the V_{OC} is further improved by PI treatment. c) Schematic diagram of the glass/ITO/HTL/perovskite/C_{60}/SnO_x stack that the trSPV measurements are performed on. d) TrSPV measurements for 3C2H and 3C3H absorbers and 3C3H with PI passivation indicating improved charge extraction at the ETL for the 3C3H absorber compared to reference 3C2H as well as future improvement by implementing PI passivation.

devices is of particular interest. However, this is challenging in two-terminal structures as there is no direct electrical access to the individual subcells and therefore subcells are relatively poorly understood. This gets even more challenging by adding further junctions.

Here, in order to get a deeper insight into the V_{OC} improvement of our triple-junction solar cells, we conducted subcell-selective PL-based iV_{OC} imaging on triple-junction devices with different top cells (reference 3C2H, 3C3H, and 3C3H with PI passivation). **Figure 8** summarizes the measured iV_{OC} images and the respective averaged global values of the individual subcells together with the V_{OC} of final triple-junction solar cells (see Figure S8, Supporting Information). This iV_{OC} imaging method has previously been developed and used to study the subcells in perovskite-based dual–junction solar cells;[36] however, this is the first time that this characterization technique has been adapted and applied to perovskite-based triple–junction solar cells.

Comparing the iV_{OC} of the subcells determined from PL measurements shows that the iV_{OC} of silicon bottom cells and middle perovskite cells in all three triple-junction structures are comparable, within the measurement uncertainty. This indicates firstly that there is not a significant device-to-device variation when integrating the subcells in the triple-junction devices. Secondly, the V_{OC} improvement in our triple-junction solar cell

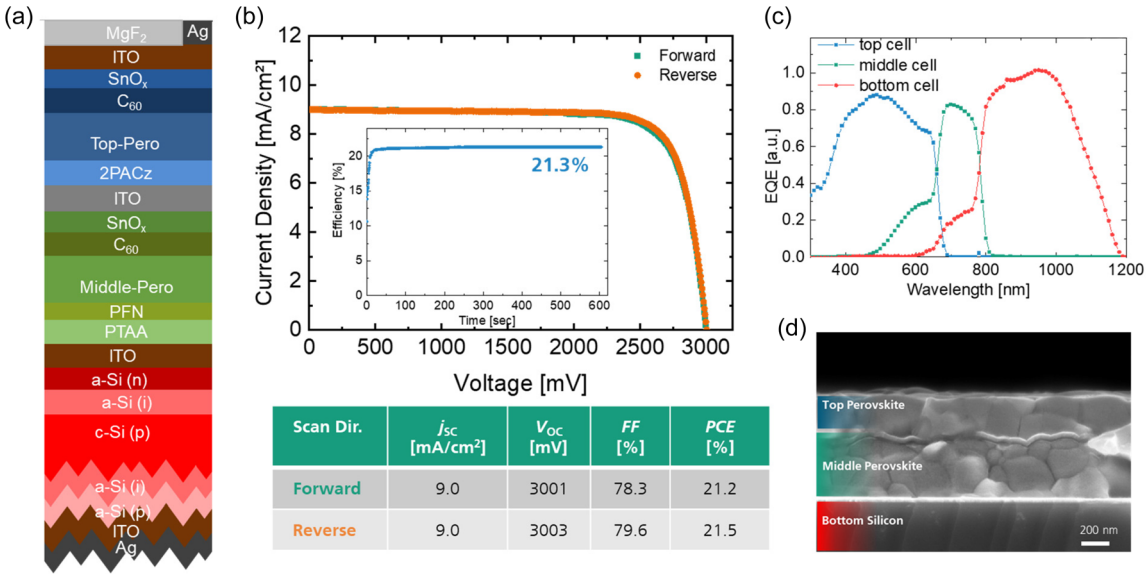

Scan Dir.	j_{SC} [mA/cm²]	V_{OC} [mV]	FF [%]	PCE [%]
Forward	9.0	3001	78.3	21.2
Reverse	9.0	3003	79.6	21.5

Figure 7. a) Schematic of the perovskite/perovskite/silicon triple-junction solar cell. b) *jV* curve of the champion solar cell together with the efficiency determined from a fixed voltage measurement (applying a constant voltage ≈V_{MPP} and tracking the current over time). c) Corresponding *EQE* of the cell. d) Cross-sectional SEM image of the triple-junction cell processed until the top perovskite absorber.

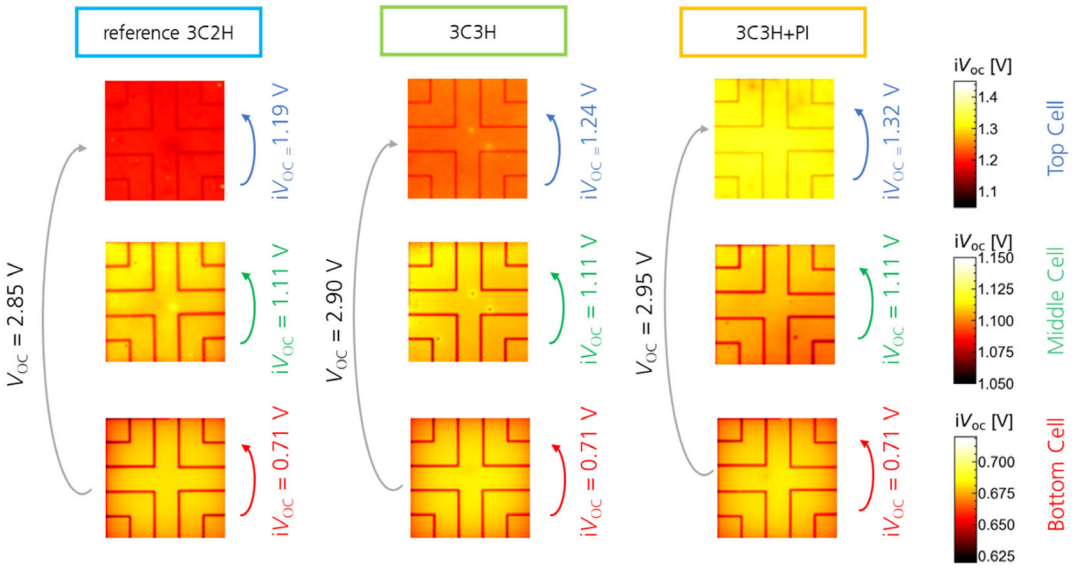

Figure 8. Subcell selective iV_{OC} images of triple-junction solar cells with 3C2H, 3C3H, and 3C3H + PI passivation as top cell. The V_{OC} of the devices are shown on the left. The iV_{OC} of the individual subcells are shown on the right. iV_{OC} measured for the bottom cells and middle cells are similar and the improved V_{OC} originated from the top cell improvement.

is the direct result of high bandgap perovskite top cell optimization. The 3C3H perovskite top cell shows a 50 mV higher iV_{OC} than the 3C2H reference and this value increases by 80 mV by implementing PI passivation. In addition to the spatially averaged iV_{OC} values of each subcell, the spatially resolved iV_{OC} images provide information on the homogeneity of each subcell. The results indicate that both the perovskite middle and top cells exhibit uniform iV_{OC} across the film.

Finally, although the average V_{OC} of our triple-junction solar cell is improved by 124 mV, it can further be improved by minimizing the remaining voltage losses in middle and top perovskite solar cells. For example, by employing charge transport layers with better band alignment especially for the high bandgap perovskite and reducing the nonradiative recombination loss at the middle perovskite/C_{60} interface, the V_{OC} of the subcells and consequently the V_{OC} of triple-junction solar cells could be further improved. Restat et al.[25] showed that assuming no Shockley–Read–Hall and surface recombination, minimum series resistances, and perfectly band-aligned ETLs/HTLs for the subcells, our triple-junction solar cell could

deliver a V_{OC} of 3.4 V. Along with maximizing the V_{OC}, one of the most important aspects with regard to the multijunction solar cells is current matching between the subcells. In order to achieve current matching and maximize the current density in our triple-junction cell, the bandgaps and thicknesses of both the middle cell and top cell should be optimized. In our champion solar cell, the silicon bottom cell generates more current compared to the two perovskite subcells.[25] Optical simulation revealed that red shifting the absorption edge of the perovskite middle cell from 1.56 to 1.47 eV results in 3 mA cm^{-2} gain in j_{SC} 25. Achieving such a low bandgap absorber requires partial substation of Pb with tin (Sn) in the perovskite composition.[11]

3. Conclusion

In summary, we have shown that the high V_{OC} deficit of high bandgap perovskites can be reduced by replacing the triple-cation/double-halide perovskite composition (3C2H) with a triple-cation/triple-halide perovskite composition (3C3H) with improved bulk quality. The target perovskite absorber shows preferred orientation toward the (112) plane with superior bulk quality and consequently enhanced iV_{OC} compared to the reference 3C2H perovskite. In addition, by adding a PI passivation layer between the perovskite/C_{60} interface, iV_{OC} can be further enhanced due to reduction of nonradiative recombination at this interface. Finally, by employing the optimized top cell, we demonstrated a perovskite/perovskite/silicon triple-junction solar cell with 3 V open-circuit voltage, which is a 150 mV improvement compared to the reference triple-junction device. The source of this V_{OC} improvement is confirmed to originate from the improved top cell using subcell-selective iV_{OC} imaging. The V_{OC} of the triple-junction solar cell can further be improved by minimizing the remaining voltage losses in subcells, particularly by employing perfectly band-aligned ETLs/HTLs.

4. Experimental Section

Materials: Methylammonium bromide (MABr) and formamidinium iodide (FAI) were purchased from GreatCell Solar. Lead bromide ($PbBr_2$), lead iodide (PbI_2), and lead chloride ($PbCl_2$) were from TCI. Cesium iodide (CsI), methylammonium chloride (MACl), PFN-Br (poly(9,9-bis(3′-(*N*,*N*-dimethyl)-*N*-ethylammoinium-propyl-2,7-fluorene)-alt-2,7-(9,9-dioctylfluorene))dibromide), and PTAA (poly[bis(4-phenyl)(2,4,6-trimethylphenyl)amine]) were from Sigma–Aldrich. 2PACz [2-(9 H-carbazol-9-yl)ethyl]phosphonic acid) and PI were from Dyenamo.

Perovskite Solution Preparation: For the preparation of the 1.83 eV triple-cation/double-halide perovskite $Cs_{0.05}(FA_{0.55}MA_{0.45})_{0.95}Pb(I_{0.55}Br_{0.45})_3$, 1.2 M $MAPbBr_3$ and $FAPbI_3$ solutions (with 10% Pb excess) in a mixture of dimethyl formamide (DMF) and dimethyl sulfoxide (DMSO) (4:1 volume ratio) and a 1.5 M CsI solution in DMSO were prepared. All solutions stirred overnight at room temperature. The $MAPbBr_3$ and $FAPbI_3$ solutions were then mixed in a 45:55 ratio and 5 vol-% of CsI was added to the final solution. The solution then diluted to 1 M. For the preparation of 1.83 eV triple-cation/triple-halide perovskite $Cs_{0.20}FA_{0.71}MA_{0.09}Pb(I_{0.64}Br_{0.27}Cl_{0.09})_3$, first the double-cation perovskite 1 M $(Cs_{0.22}FA_{0.78})Pb(I_{0.85}Br_{0.15})_3$ was prepared by mixing the stoichiometric amount of PbI_2, $PbBr_2$, FAI, and CsI with 17% $PbBr_2$ excess in DMF:DMSO (3:1 volume ratio) and stirring overnight at room temperature. Next day stoichiometric amount of MACl and $PbCl_2$ was added to the solution and stirred at 60 °C for more than 2 h.

Single-Junction Solar Cell Fabrication: ITO-coated glasses were cleaned sequentially in acetone and isopropanol (IPA) each for 10 min and dried with nitrogen gas (N_2). The samples were then treated under UV-Ozone for 15 min and transferred to a nitrogen-filled glove box. 130 µL 2PACz (0.25–0.3 mg mL^{-1} in ethanol) was spin coated on the samples for 30 s at 3000 rpm followed by annealing for 10 min at 100 °C. 150 µL perovskite solutions were deposited dynamically at 4000 rpm for 35 s with a ramp of 3 s. From 20 to 10 s to the end of the spin coating program, N_2 was blown on the spinning substrate followed by annealing for 30 min at 100 °C. For the samples with PI treatment, 100 µL of the PI solution (0.4 mg mL^{-1} in IPA) was spin coated on the samples at 5000 rpm for 30 s with a ramp of 4 s and annealed for 10 min at 100 °C. After that, the samples were washed by spin coating 100 µL IPA with the same spin-coating program and annealing for 5 min at 100 °C. For the deposition of the ETL (15 nm C_{60}), an MBraun evaporation tool was used with an evaporation rate of 0.2 Å s^{-1}. Atomic layer deposition was used for the deposition of the 20 nm SnO_x buffer layer with tetrakis(dimethylamino) tin (IV) (TDMASn) and deionized water as precursors. The 20 nm thickness is achieved by 121 cycles at a temperature of 80 °C. An Oxford cluster tool was used for the sputtering of 25 nm of ITO with argon and oxygen as sputtering gas. The deposition was done at a power of 40 W and a temperature of 50 °C. For semitransparent single-junction solar cells, a shadow mask was used that defines a 0.25 cm^2 cell active area. Finally, 200 nm thick silver (Ag) was thermally evaporated through a U-shaped busbar mask and 100 nm of magnesium fluoride (MgF_2) was thermally evaporated as an antireflection coating.

Triple-Junction Solar Cell Fabrication: Flat front and texture rear side silicon bottom cells were fabricated according to our previous publications.[37] The substrates were first cleaned by spin coating 200 µL of ethanol and dried with N_2. The substrates were treated under UV-Ozone for 15 min and transferred to a nitrogen-filled glove box. For deposition of the middle cell, 120 µL of PTAA (3 mg mL^{-1} in toluene) was spin coated at 6000 rpm for 30 s and annealed at 100 °C for 10 min. For better wettability, 60 µL of PFN was spin coated on top dynamically for 20 s at 5000 rpm. Afterward, 150 µL perovskite solution was spin coated at 4000 rpm for 35 s with a ramp of 3 s. 300 µL ethyl acetate as antisolvent was dropped on the spinning substrates 25 s to the end of the program, followed by annealing for 30 min at 100 °C. C_{60} and SnO_x layers were deposited similarly to the single-junction cells. For the middle cell, the thickness of the SnO_x layer was 30 nm which was achieved through 182 cycles. 5 nm ITO was sputtered through a shadow mask that defines a 1 cm^2 active solar cell area. The deposition of the perovskite top cell is similar to the single-junction solar cells. For the front ITO deposition, the shadow mask with 1 cm^2 cell active area was used. Ag was thermally evaporated through a mask as shown in Figure S10.

Characterization: EQE Measurements: *EQEs* were measured using our in-house setup, which includes a Xenon lamp as the light source. The light is chopped at ≈133 Hz and directed through a double-grating monochromator to produce monochromatic light. A transimpedance amplifier, connected in series, strengthens the signal and provides bias voltage during the measurements. The final signal is detected by a lock-in amplifier. The *EQE* of triple-junction devices was measured following the procedure described in refs. [3,4]. Briefly, to measure the perovskite top cell, selective infrared and red LEDs (850 and 740 nm, respectively) were used. For the middle cell measurement, a combination of blue (420 nm) and infrared LEDs were employed. The silicon bottom cell was measured under selective blue and red LEDs. A bias voltage was applied to the device for each subcell measurement, following the international standard procedure.[4] The *EQE* was recorded between 300 and 1200 nm in 10 nm increments for all three subcells. The temperature was maintained at 25 °C.

I–V Measurements: *I–V* measurements of the triple-junction solar cells were performed according to our previous publication.[7] Before *I–V* measurements were conducted, we measured the *EQE* of the cells. *I–V* measurements were conducted using a Wavelabs Sinus 220 LED solar simulator. The spectrum was adjusted in a way that each individual subcell generates the same current as it would under the Air Mass 1.5 global spectrum, using the procedure described by Chojniak et al.[38] requiring only relative *EQE*. Measurements were taken in both forward

and reverse scan directions. The voltage range was set from −100 to 3100 mV with ≈6 mV steps, and each scan took ≈50 s. The setup contained a temperature control system to maintain the temperature at 25 °C during the measurement.

For *I–V* measurement of the single-junction solar cells, a Wacom solar simulator with a Xenon lamp was used. The intensity was calibrated with a silicon reference solar cell. Similar to the procedure explained for the triple-junction solar cell, the *EQE* was measured prior to the *I–V* measurement and the spectral mismatch was considered for the intensity adjustment. The voltage was scanned from −100 to 1200 mV.

iV_{OC} Imaging: A commercial measurement system developed by Fraunhofer ISE and manufactured by Intego GmbH was used to acquire the iV_{OC} images, adapting the approach described in.[36] Two lasers and a custom-integrated LED (450, 730, and 808 nm) were used to excite the subcells selectively at ≈1 sun equivalent conditions. The images were acquired using the system inbuild camera and three bandpass filters: 675 with 50 nm full width at half maximum (FWHM) for the top cell, 800 nm with FWHM 25 nm for the middle cell, and 975 nm with FWHM 50 nm for the bottom cell.

UV-Vis Measurement: Reflectance (R) and transmittance (T) measurements were performed with a Lambda 950 spectrometer (Perkin Elmer). Measurements were done from 250 to 1200 nm with 2 nm steps. The absorptance (A) was determined from RT measurements ($A = 1 - T - R$). The bandgaps (E_g) of the perovskite were estimated from Tauc plots according to the $(\alpha h\nu)^2 \propto (h\nu - E_g)$ relation, where α is the absorption coefficient calculated from Lambert–Beer's law, h is Planck's constant and ν is the frequency.

SEM and EDX Measurement: SEM images and EDX were taken with a Schottky emission SEM (Zeiss, Auriga 60) at 5 kV for SEM and 7 kV for EDX.

XPS Measurement: The photoelectron spectra were obtained using an EnviroESCA spectrometer from Specs GmbH (Phoibos 150 near-ambient pressure analyzer, 1D Delay-Line Detector, monochromatic Al Kα radiation at 1486.6 eV, incident angle 55°). Cross-sectional profiling was done with an Ionoptika GCIB 10S (10 kV, Ar+ ion sputtering, 2×2 mm^2). The samples were prepared on a conductive carbon tape. The XPS measurements were conducted at a pressure of $<8 \times 10^{-7}$ mbar. Survey spectra were measured utilizing a pass energy of 100 eV; 20 measurement accumulations were done to obtain high-resolution spectra at a pass energy of 50 eV. The I 3*d*5/2 signal was used as binding energy reference for all samples (619.20 eV).

The data evaluation was done with CasaXPS by applying the peak fitting settings in Table S1, Supporting Information. The elemental content was gained from a semiquantitative analysis; relative sensitivity factors from CasaXPS were used.

TrPL Measurement: For transient photoluminescence measurement, samples were excited using a 515 nm diode laser with a spot size diameter of 7.5 mm and laser power of 10 mW. The pulse width is set at 250 µs. Samples are measured for 300 s.

TrSPV Measurement: TrSPV studies carrier dynamics and distinguish charge carrier extraction (appears as the rise of SPV) from recombination (appears as the decay of SPV). Also, the direction of charge carrier movement can be identified from the sign of the voltage.[35]

The samples were not encapsulated and have been excited with a femtosecond laser (Menlo BlueCut) with a wavelength of 515 nm and repetition rate of 125 kHz. The laser power was attenuated with neutral density filters to 24 pJ cm^{-2} pulse^{-1}. This corresponds to a photoexcitation of $6{\cdot}10^{14}$ carriers cm^{-3}. This carrier concentration is typical for perovskite thin films under open-circuit conditions under 1 sun illumination.

The SPV signal was measured in the configuration of a parallel plate capacitor. The capacitor is formed between the reference electrode, a quartz cylinder partially coated with SnO_2:F (reference electrode), and the sample electrode, which is adjusted to the vacuum level of the ITO of the device. As an insulator on top of the perovskite, we used a 12 µm borosilicate glass. The signal was measured via a high-impedance buffer by an oscilloscope.[39]

XRD Measurement: A Bruker D8 Advance tool with a copper anode X-ray source (K_α) was used to measure the X-ray diffraction (XRD) of perovskite thin film stacks. Measurements were recorded in the 2θ range of 5–35° with a step size of 0.02°. DIFFRAC.EVA software is used for data analysis.

Supporting Information

Supporting Information is available from the Wiley Online Library or from the author.

Acknowledgements

This work was partially supported by the European Union through the Horizon Europe project Triumph under the number 101075725 and the German Federal Ministry for Economic Affairs and Climate Action (BMWK) under contract number 03EE1132A and 03EE1132B (RIESEN). The authors would like to thank K. Fischer, J. Myers, F. Martin, J. Zielonka, J. Shaji, L. Klimmek, A. Gonzalez Abad, M. Knäbbeler-Buß and K. Zimmermann for technical and measurement support.

Conflict of Interest

The authors declare no conflict of interest.

Author Contributions

Minasadat Heydarian: conceptualization (lead); data curation (lead); formal analysis (lead); investigation (lead); methodology (lead); validation (lead); visualization (lead); writing—original draft (lead). **Athira Shaji**: data curation (supporting); formal analysis (supporting); investigation (supporting); validation (supporting); writing—review and editing (supporting). **Oliver Fischer**: data curation (supporting); formal analysis (supporting); visualization (supporting); writing—review and editing (supporting). **Michael Günthel**: data curation (supporting); formal analysis (supporting); investigation (supporting); validation (supporting); visualization (supporting); writing—review and editing (supporting). **Orestis Karalis**: data curation (supporting); formal analysis (supporting); visualization (supporting); writing—review and editing (supporting). **Maryamsadat Heydarian**: data curation (supporting); formal analysis (supporting); investigation (supporting); validation (supporting); visualization (supporting); writing—review and editing (supporting). **Alexander J. Bett**: investigation (supporting); writing—review and editing (supporting). **Hannes Hempel**: investigation (supporting); writing—review and editing (supporting). **Martin Bivour**: investigation (supporting); resources (supporting). **Florian Schindler**: funding acquisition (supporting); supervision (supporting); writing—review and editing (supporting). **Martin C. Schubert**: funding acquisition (supporting); project administration (supporting); supervision (supporting); writing—review and editing (supporting). **Andreas W. Bett**: supervision (supporting); writing—review and editing (supporting). **Stefan W. Glunz**: funding acquisition (supporting); supervision (equal); writing—review and editing (supporting). **Juliane Borchert**: funding acquisition (supporting); project administration (supporting); supervision (supporting); writing—review and editing (supporting). **Patricia S. C. Schulze**: conceptualization (supporting); investigation (supporting); project administration (supporting); supervision (equal); writing—review and editing (supporting).

Data Availability Statement

The data that support the findings of this study are available from the corresponding author upon reasonable request.

Keywords

high bandgap perovskites, open-circuit voltage losses, perovskite-based triple-junction solar cells, photovoltaics, subcell analyses

Received: September 5, 2024
Revised: December 10, 2024
Published online: January 24, 2025

[1] NREL, Best Research-Cell Efficiencies. https://www.nrel.gov/pv/assets/pdfs/best-research-cell-efficiencies-rev220126.pdf (accessed: August 2024).
[2] LONGi, LONGi sets a new world record of 33.9% for the efficiency of crystalline silicon-perovskite tandem solar cells. https://www.longi.com/en/news/new-world-record-for-the-efficiency-of-crystalline-silicon-perovskite-tandem-solar-cells/ (accessed: April 2024).
[3] S. Liu, Y. Lu, C. Yu, J. Li, R. Luo, R. Guo, H. Liang, X. Jia, X. Guo, Y.-D. Wang, Q. Zhou, X. Wang, S. Yang, M. Sui, P. Müller-Buschbaum, Y. Hou, *Nature* **2024**, *628*, 306.
[4] F. Xu, E. Aydin, J. Liu, E. Ugur, G. T. Harrison, L. Xu, B. Vishal, B. K. Yildirim, M. Wang, R. Ali, A. S. Subbiah, A. Yazmaciyan, S. Zhumagali, W. Yan, Y. Gao, Z. Song, C. Li, S. Fu, B. Chen, A. Ur Rehman, M. Babics, A. Razzaq, M. de Bastiani, T. G. Allen, U. Schwingenschlögl, Y. Yan, F. Laquai, E. H. Sargent, S. de Wolf, *Joule* **2024**, *8*, 224.
[5] F. Li, D. Wu, L. Shang, R. Xia, H. Zhang, Z. Huang, J. Gong, L. Mao, H. Zhang, Y. Sun, T. Yang, X. Sun, Z. Feng, M. Liu, *Adv. Mater.* **2024**, *36*, e2311595.
[6] H. Hu, S. X. An, Y. Li, S. Orooji, R. Singh, F. Schackmar, F. Laufer, Q. Jin, T. Feeney, A. Diercks, F. Gota, S. Moghadamzadeh, T. Pan, M. Rienäcker, R. Peibst, B. Abdollahi Nejand, U. W. Paetzold, *Energy Environ. Sci.* **2024**, *17*, 2800.
[7] M. Heydarian, M. Heydarian, A. J. Bett, M. Bivour, F. Schindler, M. Hermle, M. C. Schubert, P. S. C. Schulze, J. Borchert, S. W. Glunz, *ACS Energy Lett.* **2023**, *8*, 4186.
[8] Y. J. Choi, S. Y. Lim, J. H. Park, S. G. Ji, J. Y. Kim, *ACS Energy Lett.* **2023**, *8*, 3141.
[9] J. Werner, F. Sahli, F. Fu, J. J. Diaz Leon, A. Walter, B. A. Kamino, B. Niesen, S. Nicolay, Q. Jeangros, C. Ballif, *ACS Energy Lett.* **2018**, *3*, 2052.
[10] J. Zheng, G. Wang, W. Duan, M. A. Mahmud, H. Yi, C. Xu, A. Lambertz, S. Bremner, K. Ding, S. Huang, A. W. Y. Ho-Baillie, *ACS Energy Lett.* **2022**, *7*, 3003.
[11] M. Heydarian, M. Heydarian, P. Schygulla, S. K. Reichmuth, A. J. Bett, J. Hohl-Ebinger, F. Schindler, M. Hermle, M. C. Schubert, P. S. C. Schulze, J. Borchert, S. W. Glunz, *Energy Environ. Sci.* **2024**, *17*, 1781.
[12] S. Rühle, *Sol. Energy* **2016**, *130*, 139.
[13] E. T. Hoke, D. J. Slotcavage, E. R. Dohner, A. R. Bowring, H. I. Karunadasa, M. D. McGehee, *Chem. Sci.* **2015**, *6*, 613.
[14] M. Heydarian, C. Messmer, A. J. Bett, M. Heydarian, D. Chojniak, Ö.Ş. Kabaklı, L. Tutsch, M. Bivour, G. Siefer, M. C. Schubert, J. C. Goldschmidt, M. Hermle, S. W. Glunz, P. S. C. Schulze, *Sol. RRL* **2023**, *7*, 2200930.
[15] P. Caprioglio, J. A. Smith, R. D. J. Oliver, A. Dasgupta, S. Choudhary, M. D. Farrar, A. J. Ramadan, Y.-H. Lin, M. G. Christoforo, J. M. Ball, J. Diekmann, J. Thiesbrummel, K.-A. Zaininger, X. Shen, M. B. Johnston, D. Neher, M. Stolterfoht, H. J. Snaith, *Nat. commun.* **2023**, *14*, 932.
[16] X. Liu, Y. Guo, Y. Cheng, S. Lu, R. Li, J. Chen, *Chem. Commun.* **2023**, *59*, 13394.
[17] J. Xu, C. C. Boyd, Z. J. Yu, A. F. Palmstrom, D. J. Witter, B. W. Larson, R. M. France, J. Werner, S. P. Harvey, E. J. Wolf, W. Weigand, S. Manzoor, Maikel F. A. M. van Hest, J. J. Berry, J. M. Luther, Z. C. Holman, M. D. McGehee, *Science* **2020**, *367*, 1097.
[18] F. Yang, P. Tockhorn, A. Musiienko, F. Lang, D. Menzel, R. Macqueen, E. Köhnen, K. Xu, S. Mariotti, D. Mantione, L. Merten, A. Hinderhofer, B. Li, D. R. Wargulski, S. P. Harvey, J. Zhang, F. Scheler, S. Berwig, M. Roß, J. Thiesbrummel, A. Al-Ashouri, K. O. Brinkmann, T. Riedl, F. Schreiber, D. Abou-Ras, H. Snaith, D. Neher, L. Korte, M. Stolterfoht, S. Albrecht, *Adv. Mater.* **2024**, *36*, e2307743.
[19] S. Mariotti, E. Köhnen, F. Scheler, K. Sveinbjörnsson, L. Zimmermann, M. Piot, F. Yang, B. Li, J. Warby, A. Musiienko, D. Menzel, F. Lang, S. Keßler, I. Levine, D. Mantione, A. Al-Ashouri, M. S. Härtel, K. Xu, A. Cruz, J. Kurpiers, P. Wagner, H. Köbler, J. Li, A. Magomedov, D. Mecerreyes, E. Unger, A. Abate, M. Stolterfoht, B. Stannowski, R. Schlatmann, L. Korte, S. Albrecht, *Science* **2023**, *381*, 63.
[20] K. Xu, A. Al-Ashouri, Z.-W. Peng, E. Köhnen, H. Hempel, F. Akhundova, J. A. Marquez, P. Tockhorn, O. Shargaieva, F. Ruske, J. Zhang, J. Dagar, B. Stannowski, T. Unold, D. Abou-Ras, E. Unger, L. Korte, S. Albrecht, *ACS Energy Lett.* **2022**, *7*, 3600.
[21] J. Warby, F. Zu, S. Zeiske, E. Gutierrez-Partida, L. Frohloff, S. Kahmann, K. Frohna, E. Mosconi, E. Radicchi, F. Lang, S. Shah, F. Peña-Camargo, H. Hempel, T. Unold, N. Koch, A. Armin, F. de Angelis, S. D. Stranks, D. Neher, M. Stolterfoht, *Adv. Energy Mater.* **2022**, *12*, 2103567.
[22] Z. Liu, J. Siekmann, B. Klingebiel, U. Rau, T. Kirchartz, *Adv. Energy Mater.* **2021**, *11*, 2003386.
[23] J. Thiesbrummel, F. Peña-Camargo, K. O. Brinkmann, E. Gutierrez-Partida, F. Yang, J. Warby, S. Albrecht, D. Neher, T. Riedl, H. J. Snaith, M. Stolterfoht, F. Lang, *Adv. Energy Mater.* **2023**, *13*, 2202674.
[24] J. Wang, L. Zeng, D. Zhang, A. Maxwell, H. Chen, K. Datta, A. Caiazzo, W. H. M. Remmerswaal, N. R. M. Schipper, Z. Chen, K. Ho, A. Dasgupta, G. Kusch, R. Ollearo, L. Bellini, S. Hu, Z. Wang, C. Li, S. Teale, L. Grater, B. Chen, M. M. Wienk, R. A. Oliver, H. J. Snaith, René A. J. Janssen, E. H. Sargent, *Nat. Energy* **2024**, *9*, 70.
[25] L. Restat, C. Messmer, M. Heydarian, M. Heydarian, J. Schoen, M. C. Schubert, S. W. Glunz, *Sol. RRL* **2024**, *8*, 2300887.
[26] M. T. Hörantner, H. J. Snaith, *Energy Environ. Sci.* **2017**, *10*, 1983.
[27] M. A. Green, A. Ho-Baillie, H. J. Snaith, *Nat. Photonics* **2014**, *8*, 506.
[28] G. Niu, H. Yu, J. Li, D. Wang, L. Wang, *Nano Energy* **2016**, *27*, 87.
[29] Y. Sun, S. Yang, Z. Pang, Y. Quan, R. Song, Y. Chen, W. Qi, Y. Gao, F. Wang, X. Zhang, Y. Sun, J. Yang, L. Yang, F. Rosei, *ACS Appl. Mater. Interfaces* **2021**, *13*, 10822.
[30] N. Cho, F. Li, B. Turedi, L. Sinatra, S. P. Sarmah, M. R. Parida, M. I. Saidaminov, B. Murali, V. M. Burlakov, A. Goriely, O. F. Mohammed, T. Wu, O. M. Bakr, *Nat Commun.* **2016**, *7*, 13407.
[31] R. Szostak, S. Sanchez, P. E. Marchezi, A. S. Marques, J. C. Silva, M. S. Holanda, A. Hagfeldt, H. C. N. Tolentino, A. F. Nogueira, *Adv. Funct. Mater.* **2021**, *31*, 2007473.
[32] L. A. Muscarella, E. M. Hutter, S. Sanchez, C. D. Dieleman, T. J. Savenije, A. Hagfeldt, M. Saliba, B. Ehrler, *J. Phys. Chem. Lett.* **2019**, *10*, 6010.
[33] F. Li, X. Deng, F. Qi, Z. Li, D. Liu, D. Shen, M. Qin, S. Wu, F. Lin, S.-H. Jang, J. Zhang, X. Lu, D. Lei, C.-S. Lee, Z. Zhu, A. K.-Y. Jen, *J. Am. Chem. Soc.* **2020**, *142*, 20134.
[34] C. Barriga, S. Maffi, L. Peraldo Bicelli, C. Malitesta, *J. Power Sources* **1991**, *34*, 353.

[35] I. Levine, A. Al-Ashouri, A. Musiienko, H. Hempel, A. Magomedov, A. Drevilkauskaite, V. Getautis, D. Menzel, K. Hinrichs, T. Unold, S. Albrecht, T. Dittrich, *Joule* **2021**, *5*, 2915.
[36] O. Fischer, A. Fell, C. Messmer, R. Efinger, F. Schindler, S. W. Glunz, M. C. Schubert, *Sol. RRL* **2023**, *7*, 2300249.
[37] P. S. C. Schulze, A. J. Bett, M. Bivour, P. Caprioglio, F. M. Gerspacher, Ö.Ş. Kabaklı, A. Richter, M. Stolterfoht, Q. Zhang, D. Neher, M. Hermle, H. Hillebrecht, S. W. Glunz, J. C. Goldschmidt, *Sol. RRL* **2020**, *4*, 2000152.
[38] D. Chojniak, M. Schachtner, S. K. Reichmuth, A. J. Bett, M. Rauer, J. Hohl-Ebinger, A. Schmid, G. Siefer, S. W. Glunz, *Prog Photovoltaics* **2024**, *32*, 372.
[39] T. Dittrich, S. Fengler, *World Sci.* **2020**, 320, https://doi.org/10.1142/q0227.